than 15 min to allow for physical decay of O-15 radioactivity to background levels. All acquisitions were obtained in the two-dimensional mode (septa extended).

Data analysis

A filtered back-projection algorithm with a 6-mm Gaussian filter was used for image reconstruction. The reconstructed images had a matrix size of 128 × 128 × 47 and a voxel size of 1.84 × 1.84 × 3.38 mm, and all image data sets were resliced into short-axis images across the left ventricle [13].

Myocardial blood flow

rMBF was calculated from the injection of ^{15}O-H_2O by fitting the myocardial and arterial time-activity curve data to a single-tissue-compartment model that implemented corrections for partial-volume effects by introducing the tissue fraction. In addition, the model was corrected for spillover from the left ventricular (LV) chamber into the myocardial ROI by introducing the arterial blood volume [13]. In these experiments, the time-activity curves generated from large ROIs placed in the LV chamber were used as the input function.

Regional oxygen extraction fraction

In the "injection" study, rOEF was calculated according to Eqs. (2) and (5). In these formulations, F_{vein} was assumed to be 0.10 ml/g tissue and p was fixed at 0.90 ml/g. The blood volume image obtained from the ^{15}O-CO scan was used for the determination of V_B^{myo}. The value of $A_t(t)$ was obtained from the LV radioactivity concentration measured from the PET data set with small LV ROIs to minimize spillover from the myocardium. The calculation for the estimation of recirculating ^{15}O-H_2O was performed as previously described [16]. For the "continuous infusion" and "continuous inhalation" studies, in which a 600-s frame was regarded as steady-state, Eqs. (3) and (5) or Eqs. (3) and (4) were used for calculating rOEF, respectively.

Results

Table 1 summarizes the conditions of animals during the PET studies. The parameters were all within the physiologic range.

Figure 2 demonstrates the dynamic images obtained in the "injection", "continuous infusion", and "continuous inhalation" studies. With the injection and continuous-infusion methods, the right ventricle on the left side and the vena cava on the lower side were well delineated, whereas the left ventricle was moderately shown on the right side. The 16th frame (600~1,200 s after the initiation), which was used for steady-state analysis with the continuous-infusion method, was visibly distinct compared with all of the frames obtained with the injection method. However, with the continuous-inhalation method, neither ventricle could be depicted because of high radioactivity in the lung on the right and lower-side images.

The radioactivity in the blood pool obtained by ^{15}O-CO PET (Fig. 3g) and the gaseous volume estimated by inverse transmission data (Fig. 3h) were subtracted from the raw PET images (16th frame) with the continuous-inhalation and continuous-infusion methods, respectively (Fig. 3c and f). Both methods clearly delineated the myocardium after subtraction in comparison to the blood flow image (Fig. 3i). However, the continuous-inhalation method showed salient radioactivity on the lateral wall (Fig. 3c), whereas the continuous-infusion method showed only modest radioactivity in the myocardium (Fig. 3f). It is also notable that there was considerable radioactivity in the right ventricle with the continuous-infusion method even after the subtraction (Fig. 3f).

To further examine the differences between the continuous-infusion and continuous-inhalation methods, time-radioactivity curves during the PET scans were taken from four ROIs: the left ventricle (LV), right ventricle (RV), myocardium (Myo), and lung (Fig. 4). At the steady-state frame (600~1,200 s), the continuous-infusion method showed higher radioactivity in the RV and LV than in the myocardium (Fig. 4a), whereas the radioactivity of these regions was similar with the continuous-inhalation method (Fig. 4b). The radioactivity in LV was about two-thirds of that in RV in Fig. 4a, indicating that measurable radioactivity was excreted through the lung even after the femoral administration of ^{15}O-O_2. The lung excretion was also observed on the blood-subtracted image (Fig. 3e). Actually, there was significant radioactivity in the lung (Fig. 4a), although that was the lowest among the four ROIs. In contrast, the radioactivity in the myocardium was the lowest among the four ROIs with the continuous-inhalation method

Table 1 Physiological parameters of pigs during the PET studies

	pH	pCO_2 (mmHg)	pO_2 (mmHg)	tHb (g/dl)	O_2Sat (%)	HR (bpm)	BP (mmHg)	
							Diastolic	Systolic
Average	7.46	40.3	125.8	12.8	97.7	85	97.8	125.2
SD	0.032	2.51	16.69	1.30	1.83	19.5	10.4	19.3

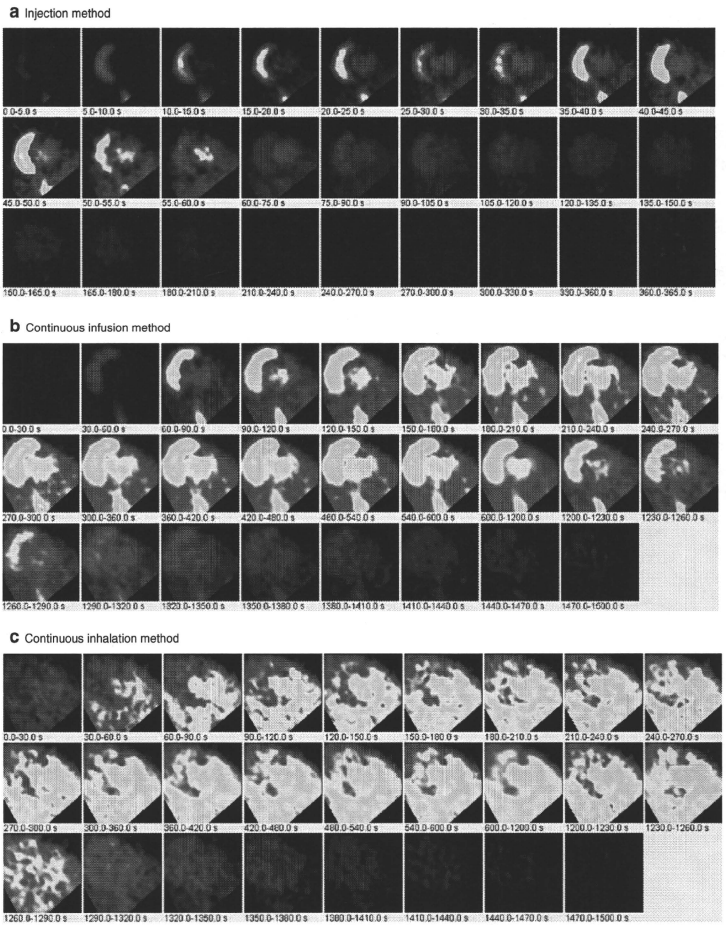

Fig. 2 PET images obtained in (**a**) the injection method, (**b**) the continuous-infusion method with injectable ^{15}O-O_2, and (**c**) the continuous-inhalation method with ^{15}O-O_2 gas

(Fig. 4b). The heart-to-lung radioactivity ratios were calculated from Fig. 4 for the quantitative estimation of image quality; the continuous-infusion method provided a ratio of 1.38±0.24, whereas the ratio was less than one with the continuous-inhalation method.

Table 2 shows the quantitative OEF values in the lateral wall obtained by the injection, continuous-infusion, and continuous-inhalation methods. These OEF values were consistent among the three methods.

Figure 5 represents the noise equivalent counts (NEC) standardized by the total counts detected by the PET scanner. Although the injection method tended to show rather high values, there was no significant difference between the values obtained by the injection and

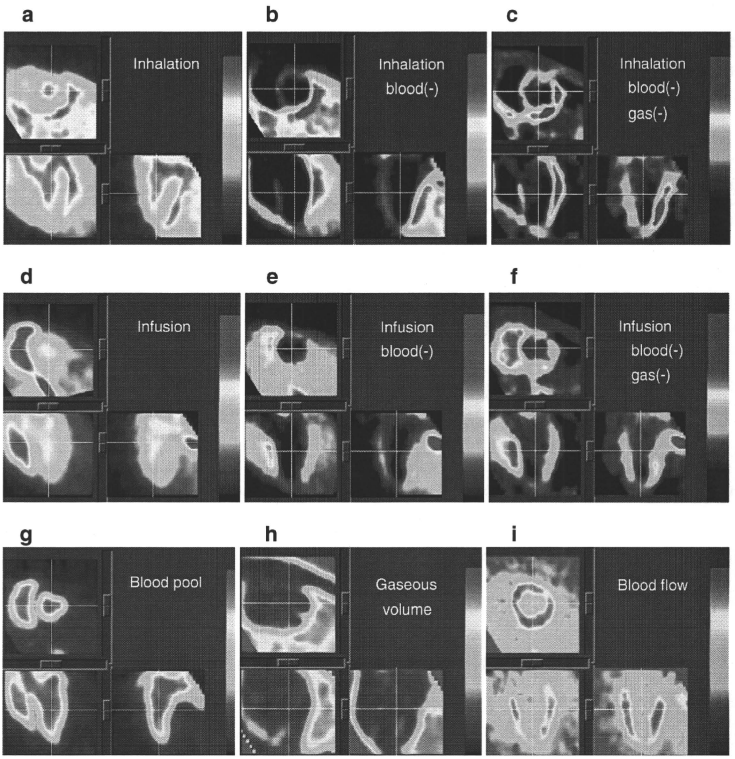

Fig. 3 PET images obtained in the study are shown. The 16th frame (steady-state frames) of the continuous-inhalation method and the continuous-infusion method are shown in (**a**) and (**d**), respectively. The 'blood-subtracted' images shown in (**b**) and (**e**) were created by subtraction of the blood-pool image by ^{15}O-CO (**g**) from (**a**) and (**d**). The 'blood- and gas-subtracted' images shown in (**c**) and (**f**) were created by the successive subtraction of the gaseous image (**h**) from (**b**) and (**e**). The myocardial blood flow image is also shown in (**i**)

continuous-infusion methods as determined by a Mann Whitney *U*-test.

Discussion

In previous studies, we showed the usefulness of the injectable ^{15}O-O_2 system for estimating cerebral oxygen metabolism in small animals such as rats under normal or ischemic conditions [10–12]. Injectable ^{15}O-O_2 replaced the inhalation protocol and radioactive ^{15}O-O_2 was administered via the tail vein. Thus, injectable ^{15}O-O_2 could abolish the artifact from the high radioactivity in the inhalation tube that distorts the PET images, especially in small animals. We considered that the concept could also be utilized in the hearts of large animals. Therefore, in the present study, we tested the feasibility of an injectable ^{15}O-O_2 system for estimating myocardial oxygen metabolism in normal pigs. In addition, since a shunt between the femoral artery and vein can be created in pigs but not in small animals, continuous infusion via the femoral shunt was also performed to achieve a constant and reliable delivery of radioactivity to the heart.

Dynamic PET scans showed a large difference in the radioactivity distribution among the three methods. Since the labeling efficiency to prepare injectable ^{15}O-O_2 was

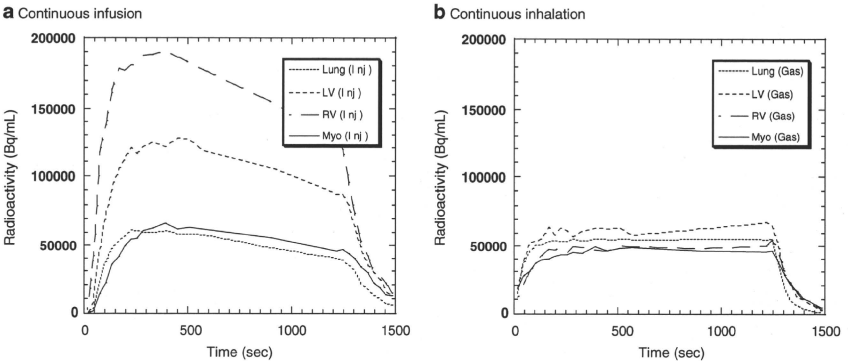

Fig. 4 Time-activity curves from the left ventricle (*LV*), the right ventricle (*RV*), the myocardium (lateral wall, Myo) and a lung region with the continuous-infusion method (**a**) and the continuous-inhalation method (**b**). The supply of radioactivity was started at time 0 s and stopped at 1,200 s. The 16th frame for the steady-state analysis was 600–1,200 s

lower with pig blood (ca. 61 MBq/ml at most) than with the blood of rats and humans (130 MBq/ml), the injection method provided rather obscure images. With the injection and continuous-infusion methods, the radioactivity in the lung was dramatically reduced in comparison to the continuous-inhalation method, since the heart-to-lung ratio with the continuous-infusion method was about 40% higher than with the continuous-inhalation method. This finding suggested that the two methods that inject radioactivity via a vein are more useful for analyzing myocardial oxygen metabolism in pigs than the continuous-inhalation method. However, a distinct difference between radioactivity of the right and left ventricles was observed in the images and time-radioactivity curves after venous administration of ^{15}O-O_2, indicating a certain degree of excretion of the radioactivity by the lung. Therefore, the spillover from the pulmonary alveoli to the myocardium could not be omitted in the two methods with venous administration, and Eq. (4) was used for the OEF analysis, although the radioactivity in the lung was lower than that in the myocardium.

On the other hand, with the continuous-inhalation method, the radioactivity of the lung was in between the radioactivity in the RV and LV. This is curious because O-15 radioactivity was supplied from the inhalation tube and transferred from the lung to blood so that the radioactivity in the lung should have been the highest among the four ROIs. This may have been caused, in part, by inhomogeneous distribution of the radioactivity in the lung due to its structure in comparison with the myocardium and ventricles, and/or by artifacts from the lung to other

Table 2 OEF estimated by the three methods using injectable ^{15}O-O_2 or ^{15}O-O_2 gas

	OEF		
	Injection	Infusion	Inhalation
Pig. 1	0.70	0.72	
Pig. 2	0.67	0.72	
Pig. 3	0.71	0.74	
Pig. 4	0.76	0.69	0.72
Average	0.71	0.72	0.72
SD	0.036	0.020	

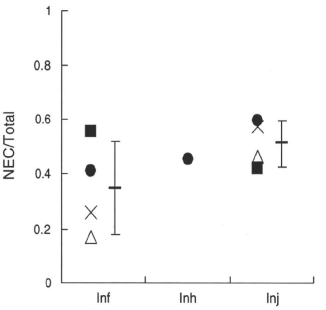

Fig. 5 The ratio of noise equivalent counts (*NEC*) to total counts in the total field of view of the PET scanner obtained with the continuous-infusion method (*Inf*), the continuous-inhalation method (*Inh*) and the injection method (*Inj*)

tissues. In any case, it is notable that the radioactivity in the myocardium was the lowest with the continuous-inhalation method, leading to difficulty in analyzing myocardial oxygen metabolism.

The OEF values in lateral walls were calculated to compare the ability of the three methods to determine myocardial oxygen metabolism by using the blood flow derived from the dual-administration protocol with the injection method and the single-administration protocol with the two continuous methods. There was no difference in the blood flow between the two protocols. Consequently, the three methods provided the same OEF value of about 0.7 and this is a physiological value in normal pigs, as was previously demonstrated [17, 18]. We have demonstrated the potential of the injectable ^{15}O-O_2 system for the estimation of physiological cerebral oxygen metabolism in rats and monkeys during early and late ischemia, hypertension, and ischemia plus hypertension [10–12, 19]. Therefore, we believe that the injection and continuous-infusion methods provide a physiological OEF in the myocardium. Nevertheless, we recognize the necessity to evaluate the reliability and usefulness of the injectable ^{15}O-O_2 method in myocardial applications. Further studies using pathophysiological animal models are required in the future, such as myocardial ischemia, hypoxia, and heart failure. On the other hand, since $MMRO_2$ is basically regarded as the product of MBF and OEF, the results indicated that these three methods were equivalent in their ability to quantify $MMRO_2$ in normal pigs, at least in the lateral wall. Although the images after the subtraction of spillovers from blood and gas showed different contrast between the continuous-infusion and continuous-inhalation methods, the ability of these two methods to measure OEF and $MMRO_2$ in the lateral walls was equivalent.

We did not evaluate myocardial oxygen metabolism in other heart regions since the radioactivity in the right ventricle could not be removed due to a significant difference of radioactivity between the ventricles with the continuous-infusion method. The injection method might be able to evaluate oxygen metabolism in other regions besides the lateral wall, although this was not evaluated in this study due to the low radioactivity of injectable ^{15}O-O_2 as described above. In the injection method, O-15 radioactivity was delivered from the femoral vein to RV, the lung, LV, and finally the myocardium. Thus, when the LV and myocardial activity reach a maximum, the RV activity is expected to be low. The later frames of the dynamic PET images with the injection method might avoid the high RV activity and delineate the myocardium and LV more clearly. With accurate anatomical information by gated PET/CT, the injection method will provide oxygen metabolism in other heart regions. In addition, the injection method has a benefit in that it is noninvasive and shortens the acquisition time in comparison with the continuous-infusion method. Future studies are needed to determine whether the injectable ^{15}O-O_2 system can be used in other heart regions.

With the injection method, the ratio of noise equivalent counts (NEC) to total counts tended to be the higher, probably because of the absence of high radioactivity adjacent to the PET scanner. Nevertheless, the continuous-infusion method did not show this tendency. This may be because tubes for the input to the artificial lung were positioned at the femoral shunt and the output to the drain of O-15 gas was positioned alongside the PET scanner, resulting in an increase of random counts during the study. Also, it is notable that the value with the continuous-inhalation method was not small, which suggests that the inhalation protocol itself did not worsen the results, but rather the high radioactivity in the lung might affect the analysis. In any case, if more care is given to shielding of the radioactivity in tubes and/or for arrangement of instruments in the PET room, a higher value of NEC/total counts will be obtained with the injectable ^{15}O-O_2 system.

The declining slope delineated in the time-activity curves with the continuous-infusion method requires some explanation. Since the flow rate of O-15 gas supply to the artificial lung positioned at the femoral shunt was maintained constant during the PET scan, it is possible that a decrease of labeling efficiency of the artificial lung occurred due to the deposition of any components of blood. The blood of rats or humans was negligibly deposited in the artificial lung during circulation at the same rate for at least 30 min in our other experiments, so that this problem may be specific for pigs. It is unclear which component in pig blood was exactly involved in the deposition and three of four pigs did not show a declining slope of the time-activity curve.

In practice, in routine studies on myocardial oxygen metabolism using large animals such as pigs, the continuous-inhalation method with ^{15}O-O_2 gas may be easier to perform for the following reasons: (1) the intubation tube used for gas anesthesia prior to the PET scan can also be used for ^{15}O-O_2 gas inhalation; (2) catheterization of the femoral artery and vein to create the femoral shunt for the continuous-infusion method may be troublesome; and (3) the injection of ^{15}O-O_2 requires an artificial lung, preparation time, and blood taken from the same animal prior to the PET scan. However, the injection of ^{15}O-O_2 has a substantial advantage over the continuous-inhalation method in that there is reduced radioactivity in the lung and clearer images of the heart are obtained. Therefore, the method for estimating myocardial oxygen metabolism should be selected depending on the objectives of the study and the surgical procedures. Furthermore, since radioactivity administered into the femoral vein is partially excreted into expired air, the injectable ^{15}O-O_2 system might be used for evaluating pulmonary function in the future.

Conclusion

In this study, we tested the feasibility of using an injectable ^{15}O-O_2 system to estimate myocardial oxygen metabolism in pigs. Both the bolus-injection and continuous-infusion methods reduced the radioactivity in the lung and provided similar OEF values in the lateral walls of the heart. These findings indicate that the injectable ^{15}O-O_2 system has the potential to evaluate myocardial oxygen metabolism.

References

1. Ohtake T. The review of myocardial positron emission computed tomography and positron imaging by gamma camera. Kaku Igaku. 1998;35:179–87.
2. Klein LJ, Visser FC, Knaapen P, Peters JH, Teule GJ, Visser CA, et al. Carbon-11 acetate as a tracer of myocardial oxygen consumption. Eur J Nucl Med. 2001;28:651–68.
3. Schelbert HR. PET contributions to understanding normal and abnormal cardiac perfusion and metabolism. Ann Biomed Eng. 2000;28:922–9.
4. Visser FC. Imaging of cardiac metabolism using radiolabelled glucose, fatty acids and acetate. Coron Artery Dis. 2001;12(Suppl 1):S12–8.
5. Hata T, Nohara R, Fujita M, Hosokawa R, Lee L, Kudo T, et al. Noninvasive assessment of myocardial viability by positron emission tomography with ^{11}C acetate in patients with old myocardial infarction. Usefulness of low-dose dobutamine infusion. Circulation. 1996;94:1834–41.
6. Yamamoto Y, de Silva R, Rhodes CG, Iida H, Lammertsma AA, Jones T, et al. Noninvasive quantification of regional myocardial metabolic rate of oxygen by $^{15}O_2$ inhalation and positron emission tomography. Experimental validation. Circulation. 1996;94:808–16.
7. Iida H, Rhodes CG, Araujo LI, Yamamoto Y, de Silva R, Maseri A, et al. Noninvasive quantification of regional myocardial metabolic rate for oxygen by use of $^{15}O_2$ inhalation and positron emission tomography. Theory, error analysis, and application in humans. Circulation. 1996;94:792–807.
8. Shidahara M, Watabe H, Kim KM, Oka H, Sago M, Hayashi T, et al. Evaluation of a commercial PET tomograph-based system for the quantitative assessment of rCBF, rOEF and $rCMRO_2$ by using sequential administration of ^{15}O-labeled compounds. Ann Nucl Med. 2002;16:317–27.
9. Mintun MA, Raichle ME, Martin WR, Herscovitch P. Brain oxygen utilization measured with O-15 radiotracers and positron emission tomography. J Nucl Med. 1984;25:177–87.
10. Magata Y, Temma T, Iida H, Ogawa M, Mukai T, Iida Y, et al. Development of injectable O-15 oxygen and estimation of rat OEF. J Cereb Blood Flow Metab. 2003;23:671–6.
11. Temma T, Magata Y, Kuge Y, Shimonaka S, Sano K, Katada Y, et al. Estimation of oxygen metabolism in a rat model of permanent ischemia using positron emission tomography with injectable ^{15}O-O_2. J Cereb Blood Flow Metab. 2006;26:1577–83.
12. Temma T, Kuge Y, Sano K, Kamihashi J, Obokata N, Kawashima H, et al. PET O-15 cerebral blood flow and metabolism after acute stroke in spontaneously hypertensive rats. Brain Res. 2008;1212:18–24.
13. Watabe H, Jino H, Kawachi N, Teramoto N, Hayashi T, Ohta Y, et al. Parametric imaging of myocardial blood flow with ^{15}O-water and PET using the basis function method. J Nucl Med. 2005;46:1219–24.
14. Iida H, Rhodes CG, de Silva R, Yamamoto Y, Araujo LI, Maseri A, et al. Myocardial tissue fraction–correction for partial volume effects and measure of tissue viability. J Nucl Med. 1991;32:2169–75.
15. Wienhard K, Dahlbom M, Eriksson L, Michel C, Bruckbauer T, Pietrzyk U, et al. The ECAT EXACT HR: performance of a new high resolution positron scanner. J Comput Assist Tomogr. 1994;18:110–8.
16. Kudomi N, Hayashi T, Teramoto N, Watabe H, Kawachi N, Ohta Y, et al. Rapid quantitative measurement of $CMRO_2$ and CBF by dual administration of ^{15}O-labeled oxygen and water during a single PET scan-a validation study and error analysis in anesthetized monkeys. J Cereb Blood Flow Metab. 2005;25:1209–24.
17. Alders DJ, Groeneveld AB, de Kanter FJ, van Beek JH. Myocardial O_2 consumption in porcine left ventricle is heterogeneously distributed in parallel to heterogeneous O_2 delivery. Am J Physiol Heart Circ Physiol. 2004;287:H1353–61.
18. Van Woerkens EC, Trouwborst A, Duncker DJ, Koning MM, Boomsma F, Verdouw PD. Catecholamines and regional hemodynamics during isovolemic hemodilution in anesthetized pigs. J Appl Physiol. 1992;72:760–9.
19. Temma T, Magata Y, Iida H, Hayashi T, Ogawa M, Mukai T, et al. Development of injectable O-15 oxygen and its application for estimation of OEF. International Congress Series, Quantitation in Biomedical Imaging with PET and MRI Proceedings of the International Workshop on Quantitation in Biomedical Imaging with PET and MRI. 2004;1265:262–65.

3-Tesla Magnetic Resonance Angiographic Assessment of a Tissue-Engineered Small-Caliber Vascular Graft Implanted in a Rat

Masashi Yamanami,[1,2] Akihide Yamamoto,[3,4] Hidehiro Iida,[3,4] Taiji Watanabe,[1,2] Keiichi Kanda,[2] Hitoshi Yaku,[2] Yasuhide Nakayama[1]

[1] Department of Bioengineering, Advanced Biomedical Engineering Center, National Cardiovascular Center Research Institute, Osaka, Japan

[2] Department of Cardiovascular Surgery, Kyoto Prefectural University of Medicine, Kyoto, Japan

[3] Department of Investigative Radiology, Advanced Biomedical Engineering Center, National Cardiovascular Center Research Institute, Osaka, Japan

[4] Department of Medical Physics and Engineering, Division of Health Sciences, Graduate School of Medicine, Osaka University, Osaka, Japan

Received 30 January 2009; revised 4 June 2009; accepted 15 July 2009
Published online 2 October 2009 in Wiley InterScience (www.interscience.wiley.com). DOI: 10.1002/jbm.b.31501

Abstract: In the development of small-caliber vascular grafts (diameter; less than 3 mm), animal implantation studies have been mostly performed by using rat abdominal aortas, and their certain patency must evaluate with sacrificing every observation periods, which is both labor-intensive and time-consuming when performing a large number of experiments. This study is the first to demonstrate the application of 3-Tesla contrast-free time-of-flight magnetic resonance angiography (TOF-MRA) in the continuous assessment of the status of a tissue-engineered vascular graft in rat. As a model graft, a single connective tubular tissue (diameter; 1.5 mm), prepared by embedding the silicone rod (diameter; 1.5 mm) into a subcutaneous pouch of a rat for 2 weeks an *in vivo* tissue-engineering, was used. The graft was implanted in the abdominal aorta (diameter; 1.3 mm) of the rat by end-to-end anastomosis. Repeated TOF-MRA imaging of the graft obtained over a 3-month follow-up period after implantation made it possible to evaluate the patency of the graft, both simply and noninvasively. It also permitted visualization of the connected abdominal aorta and renal and common iliac arteries having smaller caliber (diameter; less than 1 mm). In addition, the degree of the stenosis or aneurysm could also be detected. 3-Tesla MRA allowed the simplified and noninvasive assessment of the status on the vascular graft, including the formation of a stenosis or aneurysm, in the same rat at different times, which will be contributing to enhance the development of tissue-engineered vascular grafts even with small caliber. © 2009 Wiley Periodicals, Inc. J Biomed Mater Res Part B: Appl Biomater 92B: 156–160, 2010

Keywords: small-caliber vascular grafts; magnetic resonance angiography; animal implantation; biotube; tissue engineering

INTRODUCTION

Small-caliber arterial substitutes are needed for cardiac and peripheral revascularization procedures. For such small artery bypass grafting procedures, autologous arterial (e.g., internal thoracic artery and radial artery) or venous (e.g., saphenous vein) grafts still remain the most ideal vascular substitutes.[1,2] However, many patients do not have a vessel suitable for use owing to the poor quality, inadequate size or length, or previous harvest of such vessels. Moreover, a second surgical procedure is required to initially obtain the necessary vessel. Vascular prostheses, such as expanded polytetrafluoroethylene (ePTFE) and poly (ethylene terephthalate) (Dacron) grafts, have been used clinically for reconstructing arteries.[3] However, small-caliber (<6 mm) arterial substitutes have generally proved inadequate largely because of the formation of thromboses and intimal hyperplasia.[4,5]

Many design criteria have been proposed for the development of functional small-caliber arterial replacement grafts.[5–11] All most of all artificial vascular grafts (inner diameter, 1.5–3.0 mm) have been employed for transplantation

Correspondence to: Y. Nakayama (e-mail: nakayama@ri.ncvc.go.jp)

to rat abdominal aortas as an *in vivo* model.[6–8] Graft patency has been evaluated during the follow-up period by angiography[8] or by direct inspection at the time of removal for histological evaluation.[6,7] However, angiography requires cannulation of the carotid artery,[8] and a midline laparotomy is needed for direct inspection.[6,7] As a consequence, these methods are complex and invasive. Therefore, it is difficult to evaluate graft patency repeatedly in the same rat. Although, graft patency has also been evaluated by palpating the femoral pulse,[7] this method is subjective and uncertain.

The current imaging systems, including fluorescence antibody method, single photon emission computed tomography (SPECT),[12] laser doppler system,[13] or high-resolution ultrasound[14] for blood flow imaging in addition to magnetic resonance angiography (MRA), are powerful tool in tissue engineering field. However, it is considered that no imaging systems except for MRA fit for evaluation of the status of implanted small-caliber vascular grafts.

In clinical practice, MRI has been used as a noninvasive evaluation method for the assessment of brain blood vessels and peripheral arteries and also been widely used in preclinical research on experimental small rodents.[15–18] The studies have typically been aimed at understanding the patho-physiological status and evaluating the efficacy/side effects of newly developed treatments, such as pharmaceutical and regenerative medicine.

Our purpose in this study was to evaluate the status of a tissue-engineered vascular graft with inner diameter of 1.5 mm, clinically, repeatedly, and noninvasively in a rat implantation model. To this end, 3-Tesla contrast-free time-of-flight magnetic resonance angiography (TOF-MRA) was applied.

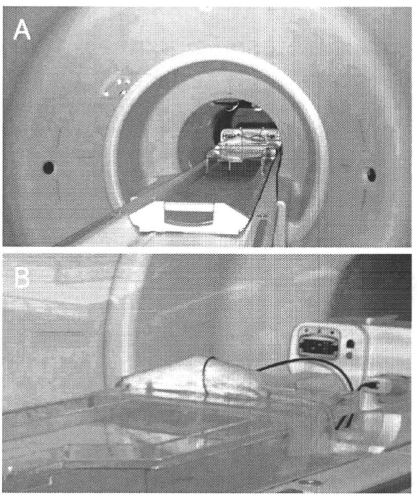

Figure 1. Experimental setup in MR imaging on a human whole-body 3T-MR scanner (GE Healthcare) (A). The coil was placed at the center of the gantry and its turn axis had perpendicular alignment to the static magnetic field (B). Rat's abdomen was positioned inside the coil along the craniocaudal direction. [Color figure can be viewed in the online issue, which is available at www.interscience.wiley.com.]

MATERIALS AND METHODS

Preparation and Implantation of the Connective Tubular Tissue

All animal experiments were conducted in accordance with local regulations, complying with the Principles of Laboratory Animal Care (formulated by the National Society for Medical Research) and the Guide for the Care and Use of Laboratory Animals (NIH Publication No. 86–23, revised 1985). The research protocol (No. 8050) was approved by the ethics committee of the National Cardiovascular Center Research Institute.

The connective tubular tissue was prepared by *in vivo* tissue engineering according to the previous reported method.[9] Briefly, a silicone rod (diameter, 1.5 mm; length, 10 mm; Tigers Polymer, Osaka, Japan) was used as a mold. One adult female Wistar rat (weight; 300 g) was anesthetized with 1.5% isoflurane (vol/vol air). The mold was placed in a dorsal subcutaneous pouch, and after 2 weeks, the implant was removed. The tubular tissue was obtained from the implant after trimming the peripheral tissues and pulling out the rod. The tube thus obtained was treated by coating with Argatroban (1 mg/graft; Mitsubishi Chemical Co., Tokyo, Japan) to make it antithrombogenic. It was then implanted to the infrarenal abdominal aorta of the same rat using an end-to-end anastomosis under microscopic guidance and sutured using 12 interrupted 10–0 nylon stitches [Figure 1(A)]. Patency was examined at the time of surgery by direct inspection. The wound was closed with 4–0 silk sutures. Thereafter, the rat had free access to standard food and water. Graft status was evaluated at 2, 36, and 78 days after transplantation by contrast-free TOF-MRA under anesthesia induced by an intramuscular injection of pentobarbital (40 mg/kg).

MR Data Acqusition

A human whole-body 3-Tesla magnetic resonance imaging (MRI) scanner (Signa, GE Healthcare, Milwaukee, WI) was employed in this study (Figure 1). The gradient coil system was capable of providing a maximum gradient amplitude of 40 mT/m. All sequence programs employed in this study were designed for clinical studies. A developed single-turn surface coil of 62 mm diameter was used for MR imaging [Figure 1(B)]. Contrast-free TOF-MRA was performed using a three-dimensional flow-compensated fast spoiled gradient recalled (3D-FSPGR) sequence [repetition

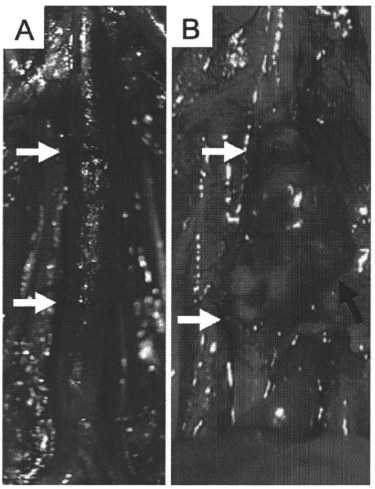

Figure 2. (A) The tubular connective tissue vascular graft (diameter; 1.5 mm) after autoimplantation in the rat infrarenal abdominal aorta (diameter; 1.3 mm) performed by end-to-end anastomosis under microscopic guidance using 12 interrupted stitches of 10-0 nylon suture. (B) The tubular connective tissue formed an aneurysm (max diameter; 3.0 mm) at 78 days after autoimplantation. White arrows indicate the proximal and distal anastomosis regions. Black arrow indicates the aneurysm. [Color figure can be viewed in the online issue, which is available at www.interscience.wiley.com.]

time (TR) = 21 ms, echo time (TE) = 5.4 ms (out of phase), flip angle (FA) = 15°, slice thickness = 0.4 mm, field of view (FOV) = 80 mm × 60 mm, matrix = 288 × 192, locs per slab = 128, the number of excitations (NEX) = 1, scanning time = 5 min 58 s]. For suppressing venous signals, a region of 40-mm thickness on the caudal side of the measured slab was saturated. The measured voxel size in TOF-MRA was 0.278 × 0.291 × 0.400 mm. The image reconstruction was zero-filled to a matrix size of 512 × 512 and the voxel size was 0.156 × 0.156 × 0.400 mm. MR angiograms were analyzed by generating the partial maximum intensity projection (pMIP) with a commercial software package (AZE, Tokyo, Japan). Our previous report on TOF-MRA was shown detail in rat.[13]

RESULTS

The tubular connective tissue with a diameter of 1.5 mm was autoimplanted successfully into the 1.3 mm diameter abdominal aorta of the rat by end-to-end anastomosis [Figure 2(A)]. After suturing with 12 interrupted stitches, there was little bleeding from either of the sites of anastomosis, indicated by the arrows in Figure 2(A). The patency of the graft was recognized directly by the satisfactory pulsation at the graft and distal side of the aorta.

3-Tesla contrast-free TOF-MRA of the rat was performed at 2 days after implantation [Figure 3(A)] to evaluate the status of the graft. The measurement time was ~6 min and no contrast medium was needed. The MRA distinctly visualized the patent graft connected to the abdominal aorta together with renal arteries and common iliac arteries of 0.7 and 0.8 mm diameter, respectively. Spatial resolution in the MRA was less than several hundred microns. A mechanical stenotic lesion, which may have been due to the anastomosis, was observed in both anastomosis regions. At 36 days after implantation, little stenosis and no aneurismal dilation of the graft were observed [Figure 3(B)]. At 78 days after implantation, the maximum diameter of the aneurysm formed at the graft was 3.0 mm [Figure 3(C)]. The shape of the aneurysm was very close to that observed macroscopically [Figure 2(B)]. Therefore, the status of the graft could be precisely determined, repeatedly, and noninvasively.

DISCUSSION

This study is the first to demonstrate the application of MRA to the evaluation of the status of a small-caliber arti-

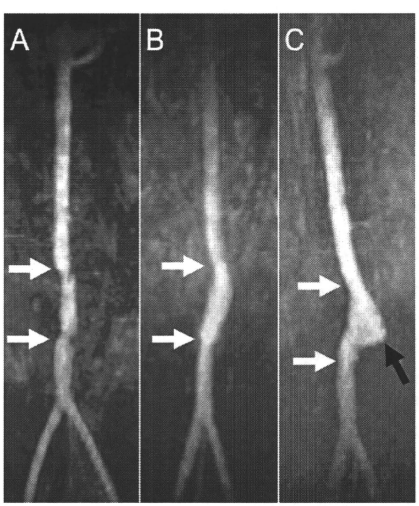

Figure 3. 3-Tesla contrast-free TOF-MRA images of the rat abdominal aorta at 2 (A), 36 (B), and 78 (C) days after autoimplantation of the biotube vascular graft. White arrows indicate the proximal and distal anastomosis regions of the abdominal aorta. A stenotic lesion was visible in the anastomosis regions at 2 days. An aneurysm formation in the graft was visible at 78 days (black arrow indicates the aneurysm).

ficial vascular graft implanted in the abdominal aorta of a rat. In the development of small-caliber vascular grafts as a preclinical study, *in vivo* evaluation is needed. Implantation studies have been performed mostly by using the abdominal aorta of rats.[6–8] Their certain patency must evaluate with sacrificing every observation periods, which is both labor-intensive and time-consuming when performing a large number of experiments. Since some rats survive with no symptoms after graft occlusion, assessment of the occlusion of an abdominal aorta after graft implantation is not possible solely on the basis of the rat's appearance. On the other hand, some researchers have evaluated graft patency by palpating the femoral pulse[7]; however, this method is prone to subjectivity and uncertainty. Therefore, evaluation of graft patency should be performed by direct inspection under laparotomy. On the other hand, even in histological observations, the evaluation of the degree of graft stenosis is very difficult.

In this study, MRI images of a reasonable quality were obtained from a rat using a human whole-body MRI scanner at 3-Tesla. Contrast-free TOF-MRA was able to depict the implanted graft with a diameter of ~1.5 mm, connected to the abdominal aorta with a diameter of ~1.3 mm, and also revealed arteries with diameters of less than 1 mm, such as the renal, common iliac, and tail arteries. In addition, an evaluation of the graft status, including the stenosis, was also feasible due to the high resolution and reasonable contrast. As indicated in Figure 3(A), the mechanical stenosis was clearly indicated at both sites of anastomosis. Furthermore, the aneurysm formation was clearly observed [Figure 3(C)]. Since the observation by MRA is simple and noninvasive, assessment of the status of small-caliber vascular grafts could be performed in the same rat at different times. The repeatable MRA observation in a single rat enabled correct assessment of the graft status over the follow-up period. Such repeatability will reduce the variation in results stemming from individual difference in experimental animals.

As a model graft for implantation in this study, the tubular connective tissue was used. The tissue was prepared similar to biotubes.[9] Biotubes are autologous prosthetic tubular tissues prepared by in-body tissue architecture technology. The biotube, obtained from rats by embedding the silicone rods (diameter; 3 mm) into their subcutaneous pouches for 4 weeks, had several 10 μm in thickness, about 500 gf in maximum load at rapture, and about 1000 mmHg in burst pressure.[19] This technology, a novel and practical concept in regenerative medicine, is based on the phenomenon of tissue encapsulation of foreign materials *in vivo*, and it can be used to develop autologous tissues of the desired shape, depending on the mold design.[9–11] Using this technology, several types of tissues, including "biotubes" as vascular tissues,[9–11] "biovalves" as tri-leaflet heart valve-shaped tissues,[20,21] and "biocovered stents" as hybrid IVR devices,[22] have been developed. In this study, by shortening of the encapsulation period weak and ununiform wall structure was prepared particularly for observation of the variety of vascular graft fate. As expected, normal, stenosis, or aneurysm models were appropriately obtained in one rat.

The assessment of graft status using MR imaging does, however, have limitations. When using certain materials for artificial grafts (e.g., ePTFE and Dacron), MR imaging might be difficult owing to graft artifacts. Furthermore, such as ultrasound and/or digital subtraction angiography, it is difficult to evaluate blood stream by 3D evaluation. The TOF-MRA is more appropriate for the evaluation of tissue-engineered vascular grafts. The signal-to-noise ratio in image quality on TOF-MRA is strongly dependent on the static field strength and the coil design. Further study should be needed in developing coil. We hope that others who study at understanding the patho-physiological status and evaluating the efficacy/side effects of newly developed treatments, such as pharmaceutical and regenerative medicine.

CONCLUSIONS

Contrast-free TOF-MRA with 3-Tesla allowed an assessment of tissue-engineered small-caliber vascular graft status in the rat systemic arterial circulation. As the protocol used in this study is simple and noninvasive, it is useful for the longitudinal evaluation of graft status in the rat; this will contribute to enhancing the development of tissue-engineered small-caliber vascular grafts, particularly in the field of regenerative medicine.

REFERENCES

1. Tomizawa Y. Vascular prostheses for aortocoronary bypass grafting: A review. Artif Organs 1995;19:39–45.
2. Ferrari ER, Von Segesser LK. Arterial grafting for myocardial revascularization: How better is it? Curr Opin Cardiol 2006; 21:584–588.
3. Zilla P, Bezuidenhout D, Human P. Prosthetic vascular grafts: Wrong models, wrong questions and no healing. Biomaterials 2007;28:5007–5027.
4. Pasquinelli G, Freyrie A, Preda P, Curti T, D'addato M, Laschi R. Healing of posthetic arterial grafts. Scanning Microsc 1990;4:351–362.
5. Isenberg BC, Williams C, Tranquillo RT. Small-diameter artificial arteries engineered in vitro. Circ Res 2006;98:25–35.
6. Doi K, Nakayama Y, Oka T, Matsuda T. A new microporous polyurethane vascular graft prepared by an excimer laser ablation technique. ASAIO J 1995;41:M608–M611.
7. Campbell JH, Efendy JE, Campbell GR. Novel vascular graft grown within recipient's own peritoneal cavity. Circ Res 1999; 85:1173–1178.
8. Pektok E, Nottelet B, Tille JC, Gurny R, Kalangos A, Moeller M, Walpoth BH. Degradation and healing characteristics of small-diameter poly (epsilon-caprolactone) vascular grafts in the rat systemic arterial circulation. Circulation 2008;118:2563–2570.
9. Nakayama Y, Ishibashi-Ueda H, Takamizawa K. In vivo tissue-engineered small-caliber arterial graft prosthesis consisting of autologous tissue (Biotube). Cell Transplant 2004;13: 439–449.

10. Sakai O, Kanda K, Ishibashi-Ueda H, Takamizawa K, Ametani A, Yaku H, Nakayama Y. Development of the wing-attached rod for acceleration of "Biotube" vascular grafts fabrication in vivo. J Biomed Mater Res B Appl Biomater 2007; 83:240–247.
11. Watanabe T, Kanda K, Ishibashi-Ueda H, Yaku H, Nakayama Y. Development of biotube vascular grafts incorporating cuffs for easy implantation. J Artif Organs 2007;10:10–15.
12. Kempen DH, Yaszemski MJ, Heijink A, Hefferan TE, Creemers LB, Britson J, Maran A, Classic KL, Dhert WJ, Lu L. Non-invasive monitoring of BMP-2 retention and bone formation in composites for bone tissue engineering using SPECT/CT and scintillation probes. J Control Release 2009; 134:169–176.
13. Hobo K, Shimizu T, Sekine H, Shin'oka T, Okano T, Kurosawa H. Therapeutic angiogenesis using tissue engineered human smooth muscle cell sheets. Arterioscler Thromb Vasc Biol 2008;28:637–643.
14. Mccarthy I. The physiology of bone blood flow: A review. J Bone Joint Surg Am 2006;88:4–9.
15. Brockmann MA, Kemmling A, Groden C. Current issues and perspectives in small rodent magnetic resonance imaging using clinical MRI scanners. Methods 2007;43:79–87.
16. Yamamoto A, Sato H, Enmi J, Ishida K, Ose T, Kimura A, Fujiwara H, Watabe H, Hayashi T, Iida H. Use of a clinical MRI scanner for preclinical research on rats. Radiol Phys Technol 2009;2:13–21.
17. Smith DA, Clarke LP, Fiedler JA, Murtagh FR, Bonaroti EA, Sengstock GJ, Arendash GW. Use of a clinical MR scanner for imaging the rat. Brain Res Bull 1993;31:115–120.
18. Guzman R, Lövblad KO, Meyer M, Spenger C, Schroth G, Widmer HR. Imaging the rat brain on a 1.5 T clinical MR-scanner. J Neurosci Methods 2000;97:77–85.
19. Huang H, Zhou YM, Ishibashi-Ueda H, Takamizawa K, Ando J, Kanda K, Yaku H, Nakayama Y. *In vitro maturation* of "Biotube" vascular grafts induced by a 2-day pulsatile flow loading. J Biomed Mater Res B Appl Biomater 2009 [Epub ahead of print].
20. Hayashida K, Kanda K, Yaku H, Ando J, Nakayama Y. Development of an in vivo tissue-engineered, autologous heart valve (the biovalve): Preparation of a prototype model. J Thorac Cardiovasc Surg 2007;134:152–159.
21. Hayashida K, Kanda K, Oie T, Okamoto Y, Sakai O, Watanabe T, Ishibashi-Ueda H, Onoyama M, Tajikawa T, Ohba K, Yaku H, Nakayama Y. "In vivo tissue-engineered" valved conduit with designed molds and laser processed scaffold. J Cardiovasc Nurs 2008;23:61–64.
22. Nakayama Y, Zhou YM, Ishibashi-Ueda H. Development of in vivo tissue-engineered autologous tissue-covered stents (biocovered stents). J Artif Organs 2007;10:171–176.

Ann Nucl Med (2010) 24:1–11
DOI 10.1007/s12149-009-0323-8

ORIGINAL ARTICLE

Development of motion correction technique for cardiac ^{15}O-water PET study using an optical motion tracking system

Kazuhiro Koshino · Hiroshi Watabe · Shinji Hasegawa · Takuya Hayashi · Jun Hatazawa · Hidehiro Iida

Received: 19 August 2009 / Accepted: 9 October 2009 / Published online: 3 December 2009

Abstract
Objective Cardiac ^{15}O-water PET studies provide an accurate quantitation of regional myocardial blood flow (rMBF). We developed a motion correction system using an optical motion-tracking device to detect a subject's global movement for cardiac study.
Methods PET studies were carried out on a cardiac phantom and a healthy volunteer at rest. The three-dimensional locations of the markers attached to the subjects during scans were measured using an optical motion-tracking system. In the phantom study, we performed a transmission scan and seven ^{18}F emission scans of a baseline and with artificial misalignment of shifts and rotations. The correlation coefficients between the baseline and the other images before and after the corrections for the misalignment were calculated. In the human study, we performed a ^{15}O-water dynamic scan with a transmission and axially 30 mm-shifted transmission scans. Motion of the subject was estimated by the information from the system, and was corrected on each sinogram using attenuation maps realigned to dynamic frames. Reconstructed dynamic images were then realigned to the transmission data. We calculated rMBF values for nine segments and myocardial images from the emission images, which were reconstructed with the first attenuation map (reference) and with the misaligned attenuation map before and after our corrections.
Results In the phantom study, the correlation coefficients were improved from 0.929 ± 0.022 to 0.987 ± 0.010 (mean ± SD) after the corrections. In the human study, the global and cyclic movements were detected. The cyclic movement due to respiration was smoothed by frame-averaging, and reasonable information of the global movement was obtained. The rMBF value (mean ± SD) was 0.94 ± 0.12 mL/min/g for the reference. The rMBF values using the misaligned attenuation map changed from 1.03 ± 0.21 to 0.93 ± 0.11 mL/min/g after the correction, and spurious defects in myocardial images were also recovered.
Conclusions Our technique provided reasonable information for correcting the global movement of the subject. It was shown that this system was applicable to detect and correct subject movement in cardiac PET studies at rest.

Keywords Myocardial blood flow · PET · Motion correction · Attenuation correction · ^{15}O-labeled water

K. Koshino (✉) · H. Watabe · H. Iida
Department of Investigative Radiology,
National Cardiovascular Center Research Institute,
5-7-1 Fujishirodai, Suita, Osaka 565-8565, Japan
e-mail: koshino@ri.ncvc.go.jp

S. Hasegawa
Department of Cardiology, Osaka Koseinenkin Hospital,
Osaka, Japan

T. Hayashi
Functional Probe Research Laboratory,
RIKEN Center for Molecular Imaging Science, Hyogo, Japan

J. Hatazawa
Department of Nuclear Medicine and Tracer Kinetics,
Osaka University Graduate School of Medicine, Osaka, Japan

Introduction

Motion of a patient during a positron emission tomography (PET) scan can cause deterioration in image quality and quantitative accuracy. Several techniques have been

proposed for motion compensation in neuroimaging [1–7]. In cardiac PET studies, effects of wall contractile and respiratory motion can be smoothed in the temporary sampled PET images, but global movement of the patients during the relatively long scanning period is still a significant source of errors [8–11].

It was shown that misalignment by a 20-mm shift in the lateral/septal direction between transmission and ^{18}F-fluorodeoxyglucose (^{18}FDG) emission scans caused a 30% change in regional activity in cardiac ^{18}F-FDG PET [8]. To align two ^{18}F-FDG emission images acquired on different days, Bacharach et al. [11] proposed a registration technique based on the rigid body model using the transmission images by assuming no misregistration between transmission and emission data sets.

Cardiac ^{15}O-water PET studies provide quantitative information with regard to the viabilities of myocardium using the myocardial blood flow (MBF), coronary flow reserve, and perfusable tissue index [12–19]. Naum et al. [20] demonstrated that the movement occurred during dynamic scans with cycling. They proposed a method to correct for the motion during a single dynamic scan, and among different sessions, by aligning the dynamic frames of ^{15}O-water images using two external radioactive markers placed on the back of a subject. Although their technique did not provide correction for misalignment between transmission and emission data, reasonable improvement in calculated MBF values was demonstrated.

Correcting the misalignment between the transmission and emission data is a challenging task because the image contrast of transmission images differs from that of emission images. The distribution of ^{15}O-water also varies dramatically in regions of the right and left ventricles, myocardium, and other organs over time. Additionally, the image quality of PET with ^{15}O-water is worse than that with other radioligands due to the short half life of ^{15}O, which makes image registration difficult.

In this paper, we describe a novel approach using an optical motion-tracking system for detecting the subject's global movement during the relatively long study period, as an extension of the early studies of Watabe et al. [4]. The proposed technique provided correction for misalignment between dynamic emission sinograms, and also provided accurate attenuation correction, in which misalignment between attenuation map and each emission sinogram was corrected in the reconstruction stage.

First, the inherent accuracy of our system was evaluated. Then, the system was validated on a cardiac phantom study for artificial misalignment between an attenuation map and emission data. Correction for global movement obtained by monitoring the locations of external markers on chest skin was validated in a ^{15}O-water cardiac PET study in a healthy volunteer at rest.

Materials and methods

Hardware-based position monitoring system

To detect motion of a subject, we adopted an optical motion-tracking device in which targets attached to the chest skin are monitored. The motion compensation approach using an optical motion-tracking system has been previously validated in brain PET studies [3–7]. We applied this approach to the cardiac PET studies. Figure 1a shows an optical motion-tracking system, POLARIS (Northern Digital Inc., Canada). The POLARIS has two charge-coupled-device cameras, and provides the 3D position of a target. The three-dimensional position is measured in the form of 6 degrees of freedom: three rotational angles, and three translational directions. The manufacturer reports that the accuracy of the rotational angle and translation are better than 0.3° and 0.5 mm, respectively. Figure 1b shows a target with four infrared-reflective markers and supporting post. The target and supporting post made of carbon resin were pinned with two fluoroplastic screws. Figure 1c shows the position calibration tool used to convert the locations of subject positions in the POLARIS coordinate into PET coordinates. Figure 1d represents the schematic diagram of our system. Locations of targets attached to the chest skin of the subject and the gantry of a PET scanner were measured with the POLARIS. The target on the gantry of the PET scanner was used as a reference in order to convert the subject's positions from the POLARIS coordinate to the PET coordinate. Figure 1e shows an example of the experimental setup with a healthy volunteer in the cardiac PET study. Two targets were attached to the chest skin of the subject. Three legs of the supporting post were attached to the skin of the subject using surgical tape. The axial field-of-view (FOV) of the PET scanner used in the human study, HEADTOME-V tomography (SHIMADZU Corp., Kyoto, Japan), was 200 mm, and the gantry diameter was 850 mm [21]. The geometries of targets attached to the thoracic surface were 85×85 mm^2 (the left-hand target in Fig. 1e, target 1) and 65×90 mm^2 (the right-hand target in the Fig. 1e). The heights of supporting posts for target 1 and target 2 were 50 and 42 mm, respectively. We calculated the subject's positions in the PET coordinate by measuring the locations of the target with four infrared-reflective markers (the primary target). Another target was used as a reserve in cases when the primary target was hidden from the FOV of the POLARIS.

Motion correction

The rigid motion correction technique employed is an extension of the previous work for brain PET studies by

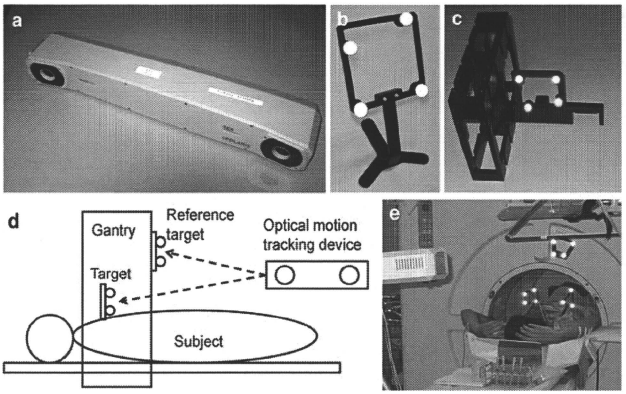

Fig. 1 Our motion correction system. **a** Optical motion-tracking device. **b** Target consists of infrared-reflective markers with supporting post. **c** Position calibration tool with a target. **d** Schematic diagram of the system. Locations of the targets on the subject and the gantry were measured with the optical motion-tracking device. **e** An example of the experimental configuration

Watabe et al. [4]. We consider four coordinates: the POLARIS C_S, a target on a PET gantry for reference C_G, a target attached on a subject C_T, and the PET scanner C_P. By measuring the location and orientation of each target attached to the subject and the gantry using the POLARIS, we obtained a 4 × 4 transformation matrixes, $T_{T\to S}$ from C_T to C_S, and $T_{G\to S}$ from C_G to C_S, respectively. Motion matrix $M_{P_1\to P_2}$ from a position $P_1 = P(t_1)$ to another position $P_2 = P(t_2)$ in the PET coordinate is written as follows [4]:

$$M_{P_1\to P_2} = T_{G\to P}T^{-1}_{G\to S}T_{T_1\to S}T^{-1}_{T_2\to S}T_{G\to S}T^{-1}_{G\to P} \quad (1)$$

where T_1 and T_2 are positions in target coordinates corresponding to positions P_1 and P_2 in the PET coordinate. $T_{G\to P}$ is the matrix to transform a position from the gantry coordinate to the PET coordinate. The matrix is given by the following equation:

$$T_{G\to P} = T_{S\to P}T_{G\to S} \quad (2)$$

$T_{S\to P}$ is the matrix which relates the POLARIS and PET coordinates and is obtained by position calibration.

The point source was embedded in a given position of a target, which is fixed on the calibration tool shown in Fig. 1c. By measuring the position of the point source using the POLARIS, the position $P_S = (x_S, y_S, z_S)$ of the point source in the POLARIS coordinate is calculated using the known position $P_T = (x_T, y_T, z_T)$ in the target coordinate and $T_{T\to S}$, as $P_S = T_{T\to S}P_T$. The position $P_P = (x_P, y_P, z_P)$ in the PET coordinate is also obtained from the reconstructed emission image. By changing the position of the target, in which the point source is embedded, $T_{S\to P}$ is calculated using the least-squared-fit between the pairs of P_Ss and P_Ps. The PET coordinate was

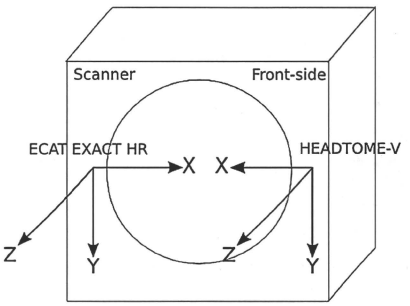

Fig. 2 PET coordinates defined by position calibrations

defined by the position calibration as shown in Fig. 2. The positions of subjects in the PET coordinate will be discussed in the following.

To correct a subject's movements during a dynamic acquisition of an emission scan with multiple frames, we estimated the heart locations from the locations of the target, which are measured by the POLARIS. The displacement of the COG of the heart's position from during the transmission scan to during each dynamic frame of the emission scan is given by

$$H^F - H^{TCT} = \frac{1}{L}\sum_t^F H(t) - \frac{1}{N}\sum_t^{TCT} H(t)$$
$$= \frac{1}{L}\sum_t^F [P(t) + \Delta(t)] - \frac{1}{N}\sum_t^{TCT} [P(t) + \Delta(t)] \quad (3)$$

where H^{TCT} and H^{F} are the averaged COGs of the heart positions during the transmission and the dynamic frame, $H(t)$ and $P(t)$ are the COGs of positions of the heart and the target at time t, $\Delta(t)$ is a term representing a non-rigid relation for positions at time t between the heart and the target, L and N are the numbers of measurements of the target's positions by the POLARIS during acquisition of the dynamic frame and the transmission scan, respectively. For motion correction, we assumed the rigid body model, in which the target and the COG of the heart's position have linear movement at least in the FOV of a PET scanner, that is, we assumed that summations of $\Delta(t)$ for the transmission scan and the dynamic frame equal to zero. The procedures of our motion-correction technique are as follows: (1) An attenuation map is aligned to the coordinate of a dynamic frame of an emission scan using the motion matrix in Eq. 1, in which P_1 and P_2 are $\Sigma^{TCT}P(t)/N$ and $\Sigma^{F}P(t)/L$ in Eq. 3. (2) The attenuation map is then converted to its sinogram by forward projection. (3) Each sinogram of the dynamic frames is reconstructed with the realigned attenuation sinogram. (4) The emission image is aligned to the transmission coordinate with the inverse matrix of the motion matrix. (5) Last, procedures from 1 through 4 are repeated for all dynamic frames of the emission data.

Position calibrations

Position calibrations were performed on two PET scanners to obtain a matrix $T_{G\to P}$ in Eq. 2, which transforms the subject's positions from a gantry coordinate to a PET coordinate. For ECAT EXACT HR tomography (CTI/Siemens, Knoxville, TN, USA) [22] used in a cardiac phantom study, ten emission scans were performed, each displaying different positions of a radioactivity point source of ^{18}F solution, using the calibration tool in Fig. 1b. For the PET scanner used in a healthy volunteer study, 14 emission scans were performed with the ^{18}F solution point source and calibration tool.

The accuracy of the calibrations was evaluated from $T_{G\to S}$ and $T_{S\to P}$ in Eq. 2. The accuracy of $T_{G\to S}$ part was evaluated by determining the standard deviation (SD) of rotational angles and translations calculated from position data of the gantry, because $T_{G\to S}$ depends on only the accuracy of the measurements in regard to the POLARIS. To evaluate the accuracy of $T_{S\to P}$ part, we calculated errors between a position of a point source P_P, and the approximation position using $T_{S\to P}$, $P_X = T_{S\to P}P_S$:

$$e(i,k) = P_X(i,k) - P_P(i,k) \tag{4}$$

$$\mathrm{RMSE}(i) = \sqrt{\sum_{k=x,y,z} |P_X(i,k) - P_P(i,k)|^2} \quad (k = X, Y, Z \text{ and } i = 1, \ldots, N) \tag{5}$$

where $e(i, k)$ is the approximation error of a point source in the ith position for each direction, X, Y, and Z are orthogonal axes in Fig. 2, RMSE(i) is the root mean square error, and N is the number of positions of a point source.

Phantom study

To validate our correction technique for the misregistration between the attenuation map and emission data, we performed PET scans using a cardiac phantom (KYOTO KAGAKU co., LTD, Kyoto, Japan, type HL-D) and the ECAT EXACT HR tomography. The phantom mimics the human thoracic region and has cardiac and liver inserts. The insert can be filled with radioisotope solution. The myocardium and liver inserts were filled with the ^{18}F solution of relative activities of 1 and 4. A target (without the supporting port) for the POLARIS was attached to the phantom using polyethylene cross tape. Then, we performed a 1,000-s transmission scan for attenuation corrections. After the transmission scan, seven ^{18}F emission scans were performed with a set of single frame data for 180 s. The first scan was the baseline (scan #1), in which there was no misalignment to the transmission. For the following three emission scans (scan #2–4), the phantom was moved in the X, Y, and Z directions. For the other three scans, the phantom was rotated about the X, Y, and Z axes (scan #5–7). The phantom's positions were measured with the POLARIS.

The reconstructed images before and after the correction were obtained using an FBP (filtered back-projection) algorithm with a Gaussian filter of 6 mm FWHM (full-width at half-maximum). The matrix size and voxel size of images were 128 × 128 × 47 and 4.4 × 4.4 × 3.1 mm^3, respectively. All emission data were corrected for physical decay of ^{18}F with base time as the start of the first emission scan, and all of the emission images were reoriented to the short axis using a transformation matrix.

To evaluate the effects of the corrections, we calculated correlation coefficients for myocardial regions between the baseline and misaligned emission images, both before and after the corrections.

Human study

A cardiac ^{15}O-water PET study was performed on a healthy volunteer (male, 32 years old) using the HEADTOME-V tomography in order to validate use of the external markers on the chest skin and also to evaluate the effects of the global movement on the quantification of MBF by artificial misalignment between attenuation and emission data. The healthy volunteer gave written informed consent according to a protocol approved by the Ethical Committee and

Internal Review Board of Osaka University. The PET study consisted of a 20-min transmission scan, an 8-min ^{15}O-CO emission scan for blood pool imaging, a 6-min ^{15}O-water emission scan with 26 dynamic frames (12 × 5, 8 × 15 and 6 × 30 s), and a second 20-min transmission scan. All scans were acquired in a 2D acquisition mode. The radioactivity of inhaled ^{15}O-CO gas was 3.2 GBq. ^{15}O-water was injected via the left brachial vein; activity was 1.1 GBq for 40 s. All scans were performed without pharmacological stress. To investigate the accuracy of the POLARIS for tracking the locations of the target attached to the thorax skin of the subject, the couch of the PET scanner was moved +30 mm along the axial direction before the second transmission scan, corresponding to the Z direction in Fig. 2, with the subject lying on the couch. It was expected that the shift in the $+Z$ direction caused the artificial deterioration of image quality and quantitative accuracy in especially the anterior and lateral regions. The subject's positions during the scans were monitored by the POLARIS, at a frequency of one sample per second.

The reconstructed images for the four cases were obtained using an FBP algorithm with a Gaussian filter of 9 mm FWHM. The matrix and voxel sizes of the reconstructed images were 128 × 128 × 63 and 2.03 × 2.03 × 3.13 mm^3. No scatter correction was performed during the image reconstruction stage.

Regional MBF values were estimated for four cases. Case 1: the first attenuation map and emission data, case 2: the first attenuation map and emission data with correction for the subject's motions, case 3: the second attenuation map and the emission data, case 4: the second attenuation map and the emission data after the correction for the subject's motions and the 30-mm-shifted misalignment. Differences in the MBF values for cases 1 and 2 were considered to indicate effects from the correction for the frame-averaged motion if the subject's motion was small. Differences in MBF values for cases 1 and 3 could indicate errors in the quantification of MBF caused by the artificial misalignment between the second attenuation map and the emission data. The lack of any difference in MBF values for cases 1 and 4 indicated that our technique tracked the shift of the target on the thorax skin accurately and corrected the misalignment. In order to generate cases 2 and 4, the positions P_1 and $P_2^{(j)}$ in Eq. 1 were calculated as averaged COGs of the subject's positions during the first and second transmission scans and the jth dynamic frame of ^{15}O-water or C^{15}O emission scan. Using Eq. 1 with P_1 and $\{P_2^{(j)}\}$, we performed frame-by-frame motion corrections for all dynamic frames of emission data. Due to the fact that the PET scanner did not provide a dynamic transmission scan, we assumed that the subject did not move during the transmission scan.

For quantification of MBF, we employed a compartment analysis model proposed by Iida et al. [13], which provided corrections for spillover from a left ventricle and partial volume effect and generated a MBF value in units of mL/min/g of perfusable tissue. All transmission and emission images were reoriented to the short axis. To calculate tissue time activity curves, regions of interest (ROIs) were drawn in nine myocardial regions: apical, mid-anterior, mid-lateral, mid-posterior, mid-septal, basal-anterior, basal-lateral, basal-posterior, and basal-septal regions. To avoid spillover effects from the right ventricle, the sizes of ROIs in septal regions were smaller than those in other regions. Another ROI was drawn on the left ventricle in order to estimate the arterial input function [19]. These ROIs were manually and independently drawn for the four cases. In addition, to validate the consistency between the quantitative results of MBF values and the quality of the images, we calculated the build-up and washout phase images [23] for the four cases. The build-up and washout phase images were obtained by subtracting a blood pool image from summed images of early (0–180 s) and later (180–360 s) frames of a ^{15}O-water image.

We evaluated the magnitude of the subject's motions in the PET coordinate during each scan. We defined position P_1 in Eq. 1 as the position at the start of the first transmission scan, and position P_2 as the position at an arbitrary time during a transmission or an emission scans. The rotational angles and translations for arbitrary times were obtained using Eq. 1. We represented motion during a scan in the form of mean ± SD for each rotational angle and translation.

Results

Position calibrations

Table 1 shows the inherent accuracy of our system in the two PET scanners. Values of SDs for rotations and translations obtained from $T_{G\to S}$ data were very small. Table 1 also shows the approximation errors (mean ± SD) occurred while transforming the positions of a point source from the POLARIS coordinate to the PET coordinate using $T_{S\to P}$. There was no bias in any direction in either scanner. Each value of RMSE was smaller than the spatial resolution of the corresponding scanner [21, 22].

Cardiac phantom study

Table 2 lists the observed misalignment from the reference position of the phantom in the transmission scan and the correlation coefficients between the reference image and the misaligned images before and after the corrections (mean ± SD; 0.929 ± 0.022 and 0.987 ± 0.010). The

Table 1 Inherent accuracy of the motion correction system in the two PET scanners

Scanner	$T_{G\to S}$						$T_{S\to P}$				# of point positions
	Rotational angle (deg)			Translation (mm)			e_x	e_y	e_z	RMSE	
	r_x	r_y	r_z	t_x	t_y	t_z					
ECAT EXACT HR	0.0	0.0	0.0	0.0	0.0	0.0	0.0 ± 0.8	0.0 ± 0.9	0.0 ± 0.8	1.3 ± 0.4	10
HEADTOME-V	0.0	0.0	0.0	0.0	0.0	0.1	0.0 ± 1.5	0.0 ± 1.6	0.0 ± 0.6	2.3 ± 0.2	14

Standard deviations of rotational angles and translations obtained from $T_{G\to S}$ data and approximation errors (mean ± SD in mm) by transforming positions of a point source from the POLARIS coordinate to the PET coordinate using $T_{S\to P}$. Columns $T_{G\to S}$, r_x, r_y and r_z denote SDs of rotational angles about three orthogonal X, Y, and Z axes, respectively. t_x, t_y and t_z denote SDs of translations along three orthogonal axes, respectively. Columns $T_{S\to P}$, e_x, e_y, and e_z denote average values (mean ± SD in mm) of $e(i, X)$, $e(i, Y)$, and $e(i, Z)$, respectively. $e(i, k)$ was defined in Eq. 4. *RMSE* denotes an average value (mean ± SD in mm) of $RMSE(i)$, defined in Eq. 5

Table 2 The observed misalignment and correlation coefficients for the phantom study

Scan no.	Rotation (deg)			Translation (mm)			Correlation coefficient	
	r_x	r_y	r_z	t_x	t_y	t_z	Before MC	After MC
2	0.0	0.2	5.1	35.7	0.8	−3.4	0.896	0.997
3	0.0	−1.0	1.3	0.9	35.2	3.2	0.938	0.995
4	0.0	−0.2	0.9	5.9	0.1	42.8	0.917	0.971
5	13.1	1.4	0.4	1.9	22.5	17.1	0.926	0.986
6	2.4	−15.6	−2.1	10.9	3.8	4.7	0.938	0.982
7	−0.6	1.8	−13.5	13.4	11.9	−9.5	0.960	0.992

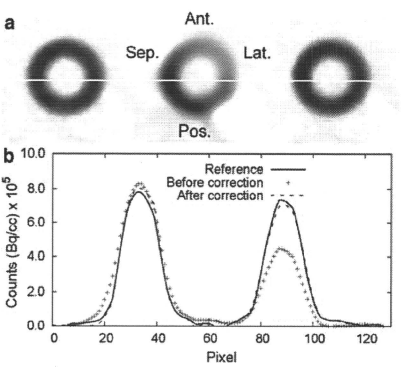

Fig. 3 Reconstructed and reoriented images of the phantom. **a** Reconstructed images. *Left*, *mid*, and *right* columns represent the reference emission image (no misalignment), the second emission images before correction for misalignment, and the second emission images after correction for the misalignment, respectively. **b** Profiles at the level of white lines in images. *Solid line*, *cross symbols*, and *dashed lines* represent the first emission image, the second emission images before correction, and the second emission images after correction, respectively

effects of our correction technique are demonstrated in Fig. 3. The left column in Fig. 3a is the reference emission image (no misalignment). The middle and right columns represent the emission images with the misalignment of the X-direction before and after the corrections. For the image in the middle column, only the position was transformed to the transmission coordinate after the reconstruction. Figure 3b represents line profiles at the level of white lines in the slices.

Human study

Table 3 summarizes the observed movements of the subject during scans relative to the beginning of the first transmission scan, in the form of rotational angles about and translations along three orthogonal axes. It was observed that the magnitude of the average parts of the rotational angles and translations tended to increase. The value of t_z changed from −1.8 ± 0.6 to 28.3 ± 0.6 mm between the ^{15}O-water emission and the second transmission scan mainly because of the 30-mm shift of the couch as well as the motions of the subject. There was little change in the SD in any rotational angle or translation among the scans.

Figure 4 shows motion parameters during ^{15}O-water scan. Figure 4a and b represent the sample-by-sample and frame-averaged translations. Figure 4c and d shows the sample-by-sample and frame-averaged rotational angles.

Table 4 shows that the MBF values (mean ± SD), which were obtained from nine myocardial segments, were 0.94 ± 0.12, 0.91 ± 0.13, 1.03 ± 0.21, and 0.93 ± 0.11 mL/min/g for the four cases. The values for cases 1 and 2 were obtained from the emission data and the first attenuation map before and after motion correction. The values for cases 3 and 4 were obtained from the emission data and the second attenuation map before and after the corrections for the subject's motions and the 30-mm shift of the couch. There were significant

Table 3 Observed movements (mean ± SD) of the healthy volunteer during scans relative to the beginning of the first transmission scan

Scan	Rotational angle (deg)			Translation (mm)		
	r_x	r_y	r_z	t_x	t_y	t_z
TCT 1	−0.1 ± 0.2	−0.4 ± 0.2	−0.2 ± 0.2	0.7 ± 0.5	1.3 ± 0.6	1.0 ± 0.8
$C^{15}O$	0.0 ± 0.2	−0.1 ± 0.2	−0.7 ± 0.1	2.6 ± 0.3	1.0 ± 0.5	−1.7 ± 0.7
^{15}O-water	0.4 ± 0.2	0.0 ± 0.1	−0.7 ± 0.1	2.7 ± 0.2	1.3 ± 0.4	−1.8 ± 0.6
TCT 2	−0.4 ± 0.2	0.7 ± 0.2	−2.0 ± 0.1	3.7 ± 0.3	2.6 ± 0.5	28.3 ± 0.6

r_x, r_y, and r_z denote rotational angles (degrees) about X, Y, and Z-axes, respectively. t_x, t_y, and t_z denote translations (mm) along X, Y, and Z axes, respectively

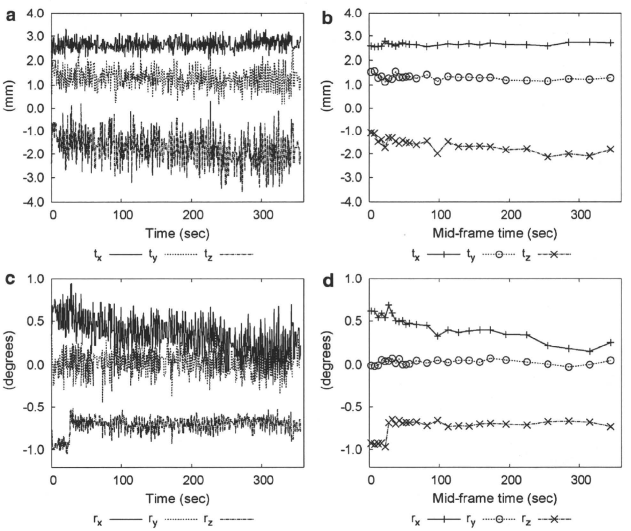

Fig. 4 Motion parameters during ^{15}O-water study on the healthy volunteer. **a**, **b** Sample-by-sample and frame-averaged translations. **c**, **d** Sample-by-sample and frame-averaged rotational angles

Table 4 MBF values (mL/min/g of perfusable tissue) of the healthy volunteer

Myocardial region	Case			
	1	2	3	4
Apical	1.05	1.00	0.99	1.05
Mid-anterior	0.92	0.89	1.26	0.99
Mid-lateral	0.93	0.89	1.38	0.89
Mid-posterior	1.14	1.16	0.96	1.01
Mid-septal	1.05	1.06	1.08	1.12
Basal-anterior	0.87	0.80	1.18	0.80
Basal-lateral	0.86	0.82	0.95	0.84
Basal-posterior	0.88	0.83	0.84	0.86
Basal-septal	0.73	0.72	0.65	0.82
Mean ± SD	0.94 ± 0.12	0.91 ± 0.13	1.03 ± 0.21	0.93 ± 0.11

differences in the mid-anterior and mid-lateral regions as well as the basal-anterior regions between cases 1 and 3.

Figure 5 demonstrates the influence of misalignment between an attenuation map and emission data on the quality of myocardial images, as well as the effect of our correction technique. Figure 5a–f represent the build-up and washout phase images of middle myocardial obtained from the ^{15}O-water data. Anterior, lateral, posterior, and septal regions of myocardia were arranged in a clockwise manner. Figure 5a and e was obtained from the data of case 1, and Fig. 5b and f was calculated from the data obtained in case 2. Figure 5c and g was derived from the data in case 3, and only positions of reconstructed images were transformed to the first transmission coordinate after reconstructions for visual

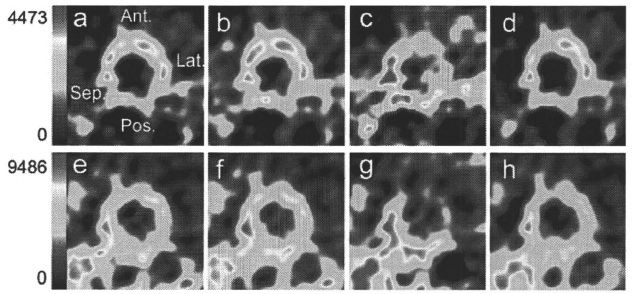

Fig. 5 Myocardial images of the healthy volunteer. **a–d** Build-up phase images. **e–h** Washout phase images. **a** and **e** were reference images obtained from data of case 1. **b** and **f** are images from data of case 2, which were corrected for the motions of the subject. **c** and **g** are images from case 3 of the emission data and the second attenuation map without our motion corrections. **d** and **h** are images from case 4, which were corrected for the motions and the misalignment between the emission data and the second attenuation map

comparison with the other images. Figure 5c and g demonstrates that reconstruction with an incorrect attenuation map caused spurious defects from anterior to lateral myocardial regions, as well as an artifact in the posterior region. Figure 5d and h is an image calculated from data obtained in case 4, in which images were also transformed to the first transmission coordinate.

Discussion

In this paper, we developed an optical motion-tracking based system to detect global movement of the subject and correct for the movement during cardiac ^{15}O-water studies.

First, the inherent accuracy of the system was assessed from position calibrations. As shown in Table 1, the $T_{G\to S}$ part could be negligibly small compared with the magnitude of the subject's motions in Table 3 and Fig. 4. For the $T_{S\to P}$ part shown in Table 1, there was no bias in any direction. The value of RMSE for each scanner was smaller than the spatial resolution of the scanner [21, 22]. Therefore, it was considered that the position calibrations provided a sufficient level of accuracy for our motion corrections.

To validate the present technique, we performed a cardiac phantom study. As shown in Fig. 3a, a defect and blurred region from the anterior to the lateral, which was mainly caused by a 5.1° rotation about the Z axis and a 35.7 mm shift along the X axis, was recovered using the present technique. The effect of the present technique was also shown more objectively by the correlation coefficients and profile comparison in Fig. 3b.

In the healthy volunteer study, no correction was applied for the motions of the subjects during the transmission scans because the PET scanners do not have the ability to perform dynamic transmission scans. Motions during a transmission scan resulted in a blurred attenuation map, and caused over- or under-estimation of the radioactive concentration in myocardium of ^{15}O-water images. However, as shown in Table 3, the magnitudes of the mean and SD during the transmission scans were smaller than the spatial resolution provided by the PET scanner, even if the magnitudes were slightly larger than those of the mean and SD during emission scans. In addition, a 9-mm smoothing filter was employed during the image reconstruction stage. Therefore, we considered that valid transmission data were acquired for the subject. For the same reason as in the case of the transmission data, the emission data of ^{15}O-water scan were acquired properly. So we used the data of case 1 as the reference for the other cases.

The global movement and cyclic movement of the target were observed as shown in Fig. 4a and c. The cyclic movement was attributed to respiration. From Fig. 4b and d, the cyclic movement was smoothed by frame-averaging. In addition, the regional MBF values (Table 4) and the myocardial images (Fig. 5) of cases 1 and 2, which were derived from the same transmission and emission scans before and after the motion correction, were nearly the same. This result indicated that our system provided reasonably accurate information about the global movement.

In case 3, in which no correction for the subject's motions and the 30-mm shift between the emission data and the second attenuation map was applied, the MBF values for the mid-anterior, mid-lateral, and basal-anterior regions were

significantly larger than the reference values. This overestimation was associated with spurious defects from the anterior to lateral regions, as shown in Fig. 5c and g. In case 4 with our correction technique, the MBF values for myocardial regions, in which overestimated MBFs were obtained for the corresponding regions in case 3, were similar to the reference values. The image quality in Fig. 5d and h was also nearly the same as in Fig. 5a and e. Figure 5d shows a clearly delineated contour of the myocardial region similar to the contour in Fig. 5a. The spurious defects from the anterior to lateral regions in Fig. 5g were recovered in Fig 5h. Owing to these results, the present technique tracked the location of the external target attached to the chest skin accurately, and then corrected the artificial misalignment during transmission and emission scans. Figure 5 not only shows the effects of our correction technique, but also suggests that the use of an attenuation map with large global movement could cause the appearance of spurious defects in myocardial imaging with ^{15}O-water PET.

Several listmode-based motion correction techniques have hitherto been proposed [1, 3–7]. Compared to these techniques, our technique provides poorer time resolution, even though our technique was applied to an emission scan consisting of dynamic frames with shorter duration. Listmode-based methods, however, require wide band transmission and high computational power for manipulating the listmode event data, especially under high count rates. For the listmode-based methods, in which data processing is conducted prior to the motion correction, corrections for detector efficiency, detector geometry, and crystal interferences are important issues, especially in the case of scanners with gaps between detectors or no intersection of motion-corrected LOR with detector(s). For our technique with 2D acquisition mode, the sinogram data are simply normalized by the built-in software of the used PET scanners. Our technique could shorten the processing time by re-binning the listmode data during the period when substantial movement is detected, and then correcting the re-framed dynamic sinogram. Furthermore, our technique is applicable to many commercially available PET scanners, which often have no feasibility of listmode acquisition.

Instead fixating the POLARIS on a certain position, such as the gantry of the PET scanner described in [3, 6], we attached the reference target onto the gantry and then used the target and the calibration tool to transform the subject's position from the POLARIS coordinate to the PET coordinate. Thus, our method allows for more flexibility in adjusting with regard to the location of the POLARIS. This is an important feature for the cardiac study due to the large inter-subject variability in the shapes of the torsos among patients, and as shown in Fig. 1e, there were enough gaps to set the best positioning for cardiac PET study. However, for exercise study, such as the studies with cycling, smaller targets and supporting post might be needed to ensure working space. An additional advantage is the portability of the POLARIS, which enables the sharing of the device among scanners in different locations.

For our technique based on the rigid body model, two targets were enough to detect the displacements and rotations of the thoraxes of the subjects, in which the secondary target was used as a reserve for cases in which the primary target was hidden from the FOV of the POLARIS. The secondary target and additional targets might be used with the corporation of the primary target to construct a non-rigid body model by detecting deformation between the chest and abdomen, and/or over the thorax region.

Another approach for the motion correction was based on image-driven information. Juslin et al. proposed an alignment technique for dynamic ^{15}O-water PET images by means of the independent component analysis. They demonstrated an improvement in quantitatively functional and parametric values, although they did not take into account for the misregistration between the transmission and emission data sets, and the movements during each emission scan [24]. The advantages of our method comparing software-based technique were (1) the misalignment between the transmission and dynamic image, and misalignment among the dynamic images could be corrected because our method was independent of the distribution and concentration of the tracer, and suboptimal image qualities (e.g., statistical noise, blurring and types of tracers). (2) Accurate attenuation correction was available because the misalignment between the transmission and the dynamic image was corrected in the reconstruction stage of the dynamic image, and (3) inherent accuracy could be obtained from the position calibration and the optical motion tracking device. Consequently, the present technique can be utilized in PET studies with several types of tracers such as ^{13}N-Ammonia and ^{18}F-FDG.

In this study, the motion correction system was demonstrated on one subject at rest. The system is to be evaluated by large population of various subjects because characteristics of motion such as magnitudes, frequencies, and directions could be different among subjects. Validation of our system is also needed for the studies during the physiologically or pharmacologically stressed conditions, in which repositioning of the heart in thoracic cavity, and larger and/or irregular (non-cyclic) chest motion by respiration would be expected. In our method, one of the limitations was correction for the misalignment due to the motion of the diaphragm with a deep breathing during a stress study, and due to the motion of the diaphragm with cough or sneezing even though during a resting study. To correct such misalignment, detection of irregular motion and a non-linear model might be needed to estimate the